

Large-Scale Organization of Ferret Auditory Cortex Revealed Using Continuous Acquisition of Intrinsic Optical Signals

Israel Nelken, Jennifer K. Bizley, Fernando R. Nodal, Bashir Ahmed, Jan W. H. Schnupp and Andrew J. King

J Neurophysiol 92:2574-2588, 2004. First published 19 May 2004;
doi: 10.1152/jn.00276.2004

You might find this additional info useful...

This article cites 46 articles, 21 of which you can access for free at:
<http://jn.physiology.org/content/92/4/2574.full#ref-list-1>

This article has been cited by 19 other HighWire-hosted articles:
<http://jn.physiology.org/content/92/4/2574#cited-by>

Updated information and services including high resolution figures, can be found at:
<http://jn.physiology.org/content/92/4/2574.full>

Additional material and information about *Journal of Neurophysiology* can be found at:
<http://www.the-aps.org/publications/jn>

This information is current as of May 24, 2013.

Large-Scale Organization of Ferret Auditory Cortex Revealed Using Continuous Acquisition of Intrinsic Optical Signals

Israel Nelken,¹ Jennifer K. Bizley,² Fernando R. Nodal,² Bashir Ahmed,² Jan W. H. Schnupp,² and Andrew J. King²

¹Department of Neurobiology and the Interdisciplinary Center for Neural Computation, The Hebrew University, Jerusalem 91904, Israel; and ²University Laboratory of Physiology, University of Oxford, Parks Road, Oxford OX1 3PT, United Kingdom

Submitted 19 March 2004; accepted in final form 13 May 2004

Nelken, Israel, Jennifer K. Bizley, Fernando R. Nodal, Bashir Ahmed, Jan W. H. Schnupp, and Andrew J. King. Large-scale organization of ferret auditory cortex revealed using continuous acquisition of intrinsic optical signals. *J Neurophysiol* 92: 2574–2588, 2004. First published May 19, 2004; 10.1152/jn.00276.2004. We have adapted a new approach for intrinsic optical imaging, in which images were acquired continuously while stimuli were delivered in a series of continually repeated sequences, to provide the first demonstration of the large-scale tonotopic organization of both primary and nonprimary areas of the ferret auditory cortex. Optical responses were collected during continuous stimulation by repeated sequences of sounds with varying frequency. The optical signal was averaged as a function of time during the sequence, to produce reflectance modulation functions (RMFs). We examined the stability and properties of the RMFs and show that their zero-crossing points provide the best temporal reference points for quantifying the relationship between the stimulus parameter values and optical responses. Sequences of different duration and direction of frequency change gave rise to comparable results, although in some cases discrepancies were observed, mostly between upward- and downward-frequency sequences. We demonstrated frequency maps, consistent with previous data, in primary auditory cortex and in the anterior auditory field, which were verified with electrophysiological recordings. In addition to these tonotopic gradients, we demonstrated at least 2 new acoustically responsive areas on the anterior and posterior ectosylvian gyri, which have not previously been described. Although responsive to pure tones, these areas exhibit less tonotopic order than the primary fields.

INTRODUCTION

Optical imaging of intrinsic signals is an important tool for functional mapping of cortical sensory areas. Maps of parameter sensitivity based on changes in intrinsic optical signals have been used to demonstrate the large-scale organization of orientation selectivity in the visual cortex (e.g., Bartfeld and Grinvald 1992; Bonhoeffer and Grinvald 1991; Frostig et al. 1990; Ts'o et al. 1990) and to study its development (e.g., Chapman et al. 1996; Weliky and Katz 1994). Optical imaging techniques have also been used to study the organization of the somatosensory cortex (e.g., Godde et al. 1995; Masino et al. 1993; Narayan et al. 1994; Tommerdahl et al. 2002) and of the olfactory system (e.g., Luo and Katz 2001; Meister and Bonhoeffer 2001; Rubin and Katz 2001). In auditory cortex, tonotopic organization that is consistent with known electrophysiology has been demonstrated in the cat (Bakin et al. 1996; Dinse et al. 1997; Spitzer et al. 2001), ferret (Versnel et al. 2002), chinchilla (Harel et al. 2000; Harrison et al. 1998), and

gerbil (Hess and Scheich 1996; Schulze et al. 2002). However, for reasons that are only partially understood, it is much more difficult to generate functional maps in auditory cortex than in visual cortex, which has so far limited the value of this technique for uncovering other organizational principles.

Illumination with long wavelengths (>700 nm) is preferred for studying visual cortex because these maximize the contribution of changes in hemoglobin oxygenation relative to the contributions of blood volume changes to the modulation of the reflectance (Frostig et al. 1990; Maloney et al. 1997; Shtoyerman et al. 2000). Because stimulus-related changes in reflectance at these wavelengths are apparently not observed, most imaging studies of auditory cortex have been conducted with green light ($\lambda \cong 546$ nm), which is thought to reflect mostly changes in blood volume (Frostig et al. 1990). However, at these shorter wavelengths, slow, local, stimulus-independent oscillations are present that can be many times larger in amplitude than the stimulus-evoked changes (Versnel et al. 2002). Consequently, maps generated using green light from auditory cortex by normalizing the averaged frames for a particular stimulus with respect to those obtained for a “null” or “blank” stimulus require long data collection times to average out the nonstimulus related signals. For example, Versnel et al. (2002) developed a successful paradigm for mapping the frequency sensitivity of auditory cortex, but this paradigm requires about 2.5 h of data collection to measure the responses to just 4 different tone frequencies.

Most of the data reported in this study were acquired using a new paradigm, similar to that used in visual cortex by Kalatsky and Stryker (2003), where images are acquired continuously and stimuli are delivered in a series of constantly repeated sequences, with each sequence running through a particular stimulus parameter of interest (e.g., up the frequency scale). This approach enabled us to use much shorter data-acquisition times and to generate functional maps from both primary and nonprimary cortical areas at much higher resolution in stimulus parameter space. The technique relies, however, on the assumption that there is a constant lag between stimulus and response, and that the major determinants of the responses are independent of the stimulation sequence. These assumptions have been recently tested in a number of studies (Martindale et al. 2003; Nemoto et al. 2004; Sheth et al. 2004) and are critically assessed here.

Address for reprint requests and other correspondence: I. Nelken, Dept. of Neurobiology, The Alexander Silberman Institute for Life Sciences, Hebrew University, Jerusalem 91904, Israel (E-mail: israel@md.huji.ac.il).

The costs of publication of this article were defrayed in part by the payment of page charges. The article must therefore be hereby marked “advertisement” in accordance with 18 U.S.C. Section 1734 solely to indicate this fact.

METHODS

Animal preparation

All animal procedures were performed under license from the UK Home Office in accordance with the Animal (Scientific Procedures) Act 1986. Seven adult pigmented female ferrets (*Mustela putorius*) were used in this study. Two of those were used in preliminary experiments; the results discussed here are from the remaining 5. Two otoscopic examinations, on the day of the experiment and 2 days before, were carried out to ensure that both ears were clean and disease free.

Anesthesia was induced by 2 ml/kg intramuscular injection of alphaxalone/alphadolone acetate (Saffan; Schering-Plough Animal Health, Welwyn Garden City, UK) and maintained, during the surgery, by intravenous injection of supplementary doses when required. Once surgery was complete, anesthesia was switched to halothane (0.5–1.5%; Merial Animal Health, Harlow, UK) with a carrier gas mixture of oxygen (50%) and nitrous oxide (50%).

Usually, the left radial vein was cannulated and a continuous infusion (5 ml/h) of saline supplemented by 5% glucose, dexamethasone (0.5 mg kg⁻¹ h⁻¹; Dexadron; Intervet UK, Milton Keynes, UK), doxapram hydrochloride (4 mg kg⁻¹ h⁻¹; Dopram-V; Fort Dodge Animal Health, Southampton, UK), and atropine sulfate (0.06 mg kg⁻¹ h⁻¹; C-Vet Veterinary Products, Leyland, UK) was maintained throughout the experiment. A tracheal cannula was implanted for artificial ventilation and gas anesthesia administration.

The animal was placed in a stereotaxic frame and the temporal muscles of both sides were retracted to expose the dorsal and lateral parts of the skull. On the right side of the skull a metal bar was cemented and screwed in place, to hold the head without further need of a stereotaxic frame. This freed the ear canals for the insertion of 2 specula into which earphones (RPHV297, Panasonic, Bracknell, UK) were fixed for acoustic stimulation. On the left side, the temporal muscle was retracted to gain access to the auditory cortex that lies ventrally to the suprasylvian sulcus (Kelly et al. 1986). The most dorsal part of the suprasylvian and pseudosylvian sulci were exposed by a craniotomy and a stainless steel chamber (16 mm diameter) was cemented and sealed around it (Fig. 1A). The overlying dura was removed and the chamber filled with silicon oil and covered with a glass plate according to procedures described by Bonhoeffer and Grinvald (1996).

A neuromuscular blocker (pancuronium bromide, 0.2 mg kg⁻¹ h⁻¹; Pavulon; N.V. Organon, Oss, The Netherlands) was added to the infusion solution to prevent involuntary movements of the animal during the acquisition of the optical imaging data. Body temperature, inspired and expired CO₂, electrocardiogram (ECG), and electroencephalogram (EEG) measurements were carefully monitored to ensure stable and adequate anesthesia.

Recordings were performed in a purpose-built, double-walled, sound-attenuated chamber. After imaging data collection was completed the glass cover and silicon oil were removed from the chamber and agar (2% in saline) was placed over the surface of the cortex for electrophysiological recordings with glass-coated tungsten electrodes.

Stimulation protocols

Stimuli constituted sequences of short (30- to 50-ms) tone bursts. Each burst consisted of a fixed-frequency tone with 5 ms ON- and OFF-ramps, and the tone frequency changed slowly from burst to burst over the sequence duration. Typically, the frequency rose continuously over a period of several seconds (4–28, most commonly 12–14 s). Identical sequences were repeated in a continuous loop to produce continuous stimulation. Because of technical limitations, data were collected in sets of 600 frames, which, at the frame rate used most commonly (240 ms/frame), lasted 144 s. Usually, these continuous stimulation periods were repeated 10 times. Thus a total of approximately 25 min of data were collected for each sequence.

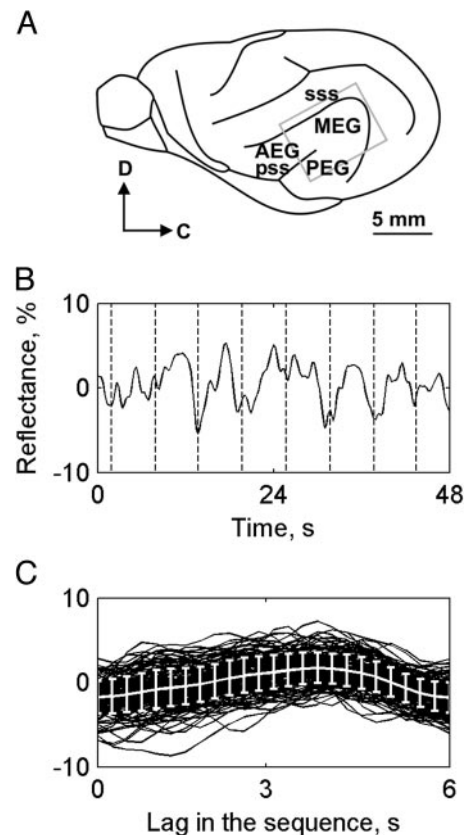


FIG. 1. *A*: schematic of the left ferret cortex. Rectangle shows the typical location of the region of auditory cortex that was imaged. Same orientation is used in the maps that appear in later figures. Abbreviations: sss, suprasylvian sulcus; pss, pseudosylvian sulcus; AEG, MEG, PEG, anterior, middle, and posterior ectosylvian gyrus, respectively. *B* and *C*: analysis of the optical signal. *B*: plot of the raw optical signal, after correction for the respiration artifacts, measured with a sequence of pure tones (duration: 6 s). Dashed vertical lines mark successive starting points of the repeated stimulus sequence. *C*: all the raw waveforms aligned on the beginning of the sequence. Total duration of the data is 870 s, corresponding to 145 repeats of the sequence. Average and SDs at each point within the sequence are overlaid in white.

The number of frequencies used varied somewhat between experiments. Frequencies were uniformly distributed on a logarithmic scale, with 12 frequencies per octave, between 500 Hz and about 30 kHz (the precise upper limit depended on the quality of the acoustic calibration in each specific animal, and varied between 28 and 32 kHz). The rate of presentation of individual tone pips then depended on the total duration of the sequence. Tone sequences of rising frequency were used in all experiments and, in some experiments, downward sequences were used as well.

Tone level was 75 dB SPL, independent of frequency. To achieve this tone level at all frequencies, a calibration was performed in each ear against a precalibrated microphone. Tone levels were adjusted using the calibration curve to achieve the nominal level.

Data collection

Intrinsic optical signals were acquired using Imager 2001VSD+ (Optical Imaging, Mountainside, NJ). In all animals, most of the data were collected while the cortex was illuminated by narrow-band green light ($\lambda = 546$ nm; 50%-bandwidth, 10 nm; Coherent-Ealing filter; Ealing Electro-Optics, Holliston, MA) directed through 2 fiber-optic light guides. In all experiments, at least one block of data was also collected with red illumination ($\lambda = 700$ nm), and in one experiment

optical signals were also collected using orange light ($\lambda = 610$ nm). The data collected with red illumination did not show any significant responses, and the data collected in orange illumination showed small areas of significant responses with much weaker stimulus sensitivity than that under green illumination. Therefore all the data presented herein were collected under green illumination.

Images were acquired using a video camera (CS8310C, Tokyo Electronic Industries, Tokyo, Japan), mounted above the cortex and perpendicular to its surface. The area over which data were collected measured approximately 8×6 mm, at 1/4 or 1/9 of the maximal resolution (758×568 pixels). Blood vessel artifacts at the cortical surface were reduced using a macro double-lens configuration [2 Nikon, 50-mm SLR camera lenses (Nikon, Tokyo, Japan) mounted front to front] with a shallow depth of field and focused $500 \mu\text{m}$ below the cortical surface. We used the VDAQ/NT data-acquisition software (v1.5, Optical Imaging).

To synchronize the auditory stimulation and the optical image acquisition, we used a separate computer that collected all the necessary timing information using AlphaMap (Alpha Omega, Nazareth, Israel). The same computer also recorded the times of every stroke of the respirator and the waveform of the ECG. The nominal period between images was 80 ms in one experiment and 240 ms in the other 4 experiments. These acquisition rates were sufficiently fast for the slow dynamics of the intrinsic optical signals (Martindale et al. 2003). The precise times of image acquisitions fluctuated somewhat around these values. Usually, this jitter was small. Thus in the 4 experiments with a period of 240 ms, the median interval was 241.8 ms (against a nominal value of 240 ms), and in all blocks, 99% of the intervals were within <17 ms of each other (about 7% of the nominal interval). The larger intervals usually occurred at the beginning of a data collection run, and were about twice as long as the nominal interval. Thus although the jitter had to be corrected, simple interpolation at equally spaced time points was sufficient for this purpose.

In 3 experiments (F0230, F0234, and F0242), data were also collected using fixed stimuli, according to the paradigm developed by Versnel et al. (2002). Four frequencies (1, 2.8, 8, and 16 kHz) were used in these experiments, interleaved with a fifth, silent, condition. Each trial lasted 17.5 s, during which 14 data frames were acquired. A total of 64 repeats were averaged for each stimulus. The stimuli consisted of four 250-ms tone pips presented once every 500 ms and were triggered 1.5 s after the beginning of the acquisition of the optical signal.

Electrophysiology

Extracellular recordings were made using fixed arrays of 4 tungsten-in-glass electrodes. The signals were band-pass filtered (500 Hz–5 kHz), amplified ($\leq 10,000\times$), and digitized at 25 kHz. Data were collected and analyzed using BrainWare (TDT, Alachua, FL). Single units and small multiunit clusters were isolated from the digitized signal. Pure tones ranging from about 0.5–30 kHz and about 10–90 dB SPL were presented pseudorandomly at a repetition rate of once per second with 5–10 repetitions per recording.

All data presented are from units whose spike counts during the stimulus were significantly different from the spike counts in windows of the same duration just before stimulus onset ($P < 0.05$, paired t -test). Units were classified as tuned if a one-way ANOVA on the evoked spike counts showed a significant ($P < 0.05$) effect of frequency. Best frequency (BF) was defined as the frequency with the lowest threshold, as measured by spike counts.

Data analysis

The images acquired in response to the continuous stimulation sequences were analyzed on a pixel-by-pixel basis. We refer to the time series of reflectance values observed at one particular pixel as the pixel's "optical waveform." Because the optical reflectance changed

only slowly over the cortical surface, the images were spatially downsampled by a factor of 3. The first step in the analysis of the optical waveform was to correct for respiration artifacts. For the experiment with the fast sampling rate, heart rate artifacts were corrected as well. For the experiments with the slower frame-acquisition rate, heart rate (250–300/min, equivalent to about 4–5/s) was about as fast as the frame rate and therefore no correction was needed. Because the algorithm used in both cases was the same, it will be described for the respiration artifacts only.

For each pixel, an average postinspiratory optical signal was determined by averaging the segments between successive ventilator strokes (about 30/min, equivalent to 0.5/s or about 8–9 frames between successive ventilator strokes). To correct for the jitter in the intervals between frames, the optical signal was resampled (using linear interpolation between nearby sample points) at the nominal frame rate, with the zero time of the resampled signal always precisely at an inspiratory event.

The respiratory averaged waveform was then convolved with the sequence of inspiratory event times (considered as delta functions) and subtracted from the raw optical waveform. Because of the jitter in the intervals between frames, the convolution was performed by resampling the average postinspiratory signal at the actual delays at which the frames occurred after an inspiratory event.

After correction for respiratory (and, where necessary, heart-beat) artifacts, the optical waveforms were normalized, by expressing them as a proportion of the average reflectance value for each pixel across the entire recording time. All further analysis was performed on the corrected, normalized frame sequences.

From the normalized signal we then calculated the stimulus-dependent reflectance modulation function (RMF) by averaging all the signal segments after the start of a stimulus sequence. Because of the jitter in the intervals between frames, the RMFs were calculated by resampling the normalized optical signal at fixed times beginning at the start of each stimulus sequence, with a resampling period approximately equal to the nominal sampling period of the optical signal (either every 80 or every 240 ms, depending on the experiment). Because the times between stimulus sequence starting points were generally not an exact multiple of the sampling period of the optical signal, the resampling rate of the optical waveform was adjusted slightly, either up or down, to accommodate an exact number of sampling points between 2 successive starts of the stimulus sequence. To judge the statistical significance of the stimulus-evoked modulation, a one-way ANOVA was performed, with the time after the start of the sequence as the factor. In all figures, only pixels with ANOVA F values >2 are displayed. The F -value represents the ratio of the variance of the RMF as a function of time over the average variance of the responses to individual cycles around this mean. It is therefore a "signal to noise ratio", and the value of 2 is a reasonable cutoff point. The significance of this F -value with respect to the null hypothesis of no modulation is <0.01 for all tests performed here, and <0.0001 for the typical tests (sequences of 12 s). Because the parameter maps most often contain about 5,000 pixels, the use of such significance levels would, on average, result in at most 50 pixels (but most commonly <1 insignificant pixel) being displayed.

Figure 1 illustrates how the RMF is extracted from the optical waveform. A short segment of the optical waveform is shown in Fig. 1B. The individual waveform segments between successive starts of the stimulus sequence are shown in Fig. 1C, with the mean waveform and SDs superimposed. The SDs are essentially independent of the lag during the stimulus sequence, justifying the use of one-way ANOVA for detecting significant modulation of the means. In this case, the modulation was highly significant [$F(24,3600) = 56.1, P < 0.001$].

For the experiments in which fixed stimuli were used, the data were analyzed as in Versnel et al. (2002). Significant response in a pixel was defined as a decrease in reflectance of more than 1 SD. The SD was first computed for each stimulus and each pixel separately, and the median of all stimuli and pixels was used for the significance test.

Each pixel was assigned to the frequency that elicited the highest peak reflectance change, provided that at least one frequency gave rise to a significant response. However, in many cases more than one frequency gave rise to a significant response, and sometimes the responses to 2 or more frequencies were of comparable magnitudes. An additional way of quantifying the sensitivity of a pixel was therefore used: all the frequencies that gave rise to a significant response in a pixel were averaged, with weights proportional to the peak activation they elicited.

Statistical tests are considered significant when $P < 0.05$. For tests resulting in extreme values of the statistics, smaller bounds on the P -values are reported.

RESULTS

In the ferret, the suprasylvian sulcus (sss) proceeds around the tip of the temporal lobe, and forms the dorsal and posterior border of auditory cortex (Fig. 1A). Primary auditory cortex (A1) occupies part of the middle ectosylvian gyrus (MEG), with low frequencies represented more ventrally and high frequencies more dorsally, often close to the tip of the sss. More ventrally, the pseudosylvian sulcus (pss) separates the MEG into the anterior and posterior ectosylvian gyri (AEG and PEG). The pattern of sound-evoked 2-deoxyglucose labeling (Wallace et al. 1997) suggests that both AEG and PEG contain auditory fields. In this study, we imaged the area centered at the tip of the pss, to include both the primary fields (A1 and AAF) and the putative ventral fields on the AEG and PEG.

Optical data were collected in 5 ferrets. Because the use of continuous stimulation is new, we will start by reporting on a number of methodological issues, including the statistical stability of the stimulus-locked signal and the effect of varying stimulation parameters, before describing the spatial distribution of frequency sensitivity observed.

Nature of the stimulus-locked signal

Under green ($\lambda = 546$ nm) illumination, the acoustic stimuli could evoke a modulation of the optical reflectance signal of $\leq 15\%$ of the mean value. However, modulations of 1–5% were more typical, even for the pixels that exhibited the strongest modulation. The stimulus-locked signal had a complex dependency on the stimulation parameters, as will be shown below. Therefore as a first step in the analysis of this signal, we studied its stability over time within and across blocks.

To study the stability of the stimulus-locked signal during a data collection block, partial RMFs were computed on short sections of about 1 min and compared with the full RMF computed over the whole recording time, which is the average of the partial RMFs. Figure 2 shows 4 examples of the evolution of the partial RMFs in single pixels from 3 animals. These data span the range of behaviors that we observed.

Figure 2A shows an example of a highly stable recording. The partial RMFs (black) were all similar to each other, and no systematic change in shape was observed as a function of time. To quantify this stability, the partial RMFs were correlated with the full RMF (red). The correlation coefficients in this case are plotted in the *inset*, and were >0.9 .

Figure 2B shows a case in which a number of partial RMFs at the beginning of the block had a shape different from that of the rest. These partial RMFs are drawn in green lines, whereas

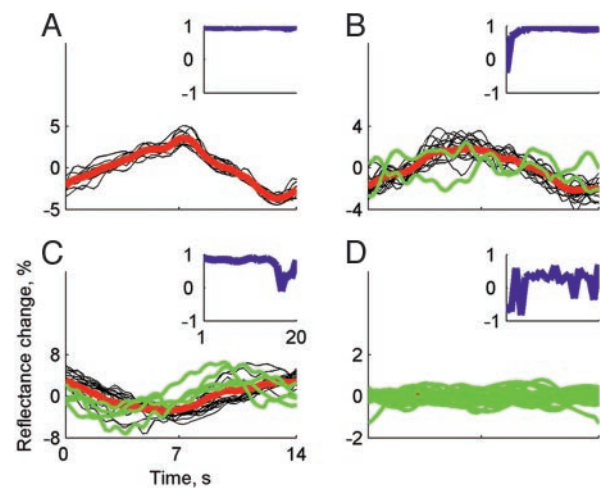


FIG. 2. Stability analysis of the optical signals. In each panel, the black lines represent the partial reflectance modulation functions (RMFs) (averaged over successive, nonoverlapping 1-min periods) and the red line is the full RMF. *Inset*: correlation coefficients between the partial and the full RMF as a function of the order of the partial RMFs. Green lines represent partial RMFs whose correlation coefficient with the full RMF was <0.75 . *A*: data from a pixel showing stable entrainment of the optical signal by the sensory stimulation throughout the block (F0242, upward-frequency sequence, 14 s, $F = 93$). *B*: data from a pixel showing a buildup of the entrainment at the beginning of the block, followed by stable entrainment (F0253, upward-frequency sequence, 14 s, $F = 35$). *C*: data from a pixel in which the phase of the optical signal changed for a few minutes toward the end of the block (F0242, downward-frequency sequence, 14 s, $F = 31$). *D*: data from a pixel in which there was no significant modulation of the optical signal by the stimulus (F0256, upward-frequency sequence, 14 s, $F = 0.5$). F values correspond to the ANOVA analysis for the full RMF.

the rest are in black. The correlation coefficient between the full RMF and the partial RMFs is small at the beginning of the block, but after 2 min it is already >0.75 and it remains large to the end of the block. Clearly, the optical signal was not locked to the stimulus at the beginning of the block. After a few cycles, however, it was entrained by the acoustic stimulation and remained highly entrained until the end of the block.

Figure 2C shows a case where the partial RMFs at the end of the block (green) had a shape different from that of the rest.

Finally, Fig. 2D shows a case in which there was no entrainment of the optical signal by the acoustic signal. The lack of entrainment is mirrored by the small F -value in this case ($F = 0.5$). The correlation coefficients between the partial RMFs and the full RMF are all <0.75 .

To quantify these phenomena, we examined the correlation coefficients between the partial and full RMFs (blue lines in the *insets* in Fig. 2) using 2 measures, the mean size of the correlation coefficients and their SD, computed on a pixel-by-pixel basis. Pixels with consistent RMFs are expected to have large mean correlation coefficient and small SD. Increase in SD is expected to occur in cases such as those illustrated in Fig. 2, B and C.

To illustrate this, Fig. 3 shows population distributions for mean correlation coefficients and SDs. The data are taken from all frequency sequence blocks from all 5 experiments. Each panel shows a histogram computed for pixels with $F > 2$ (blue), corresponding to significant modulation of the RMFs, and a histogram computed for pixels with $F < 2$ (green). The mean correlation coefficients between the partial RMFs and the full RMF (Fig. 3A) are clearly shifted to larger values in those

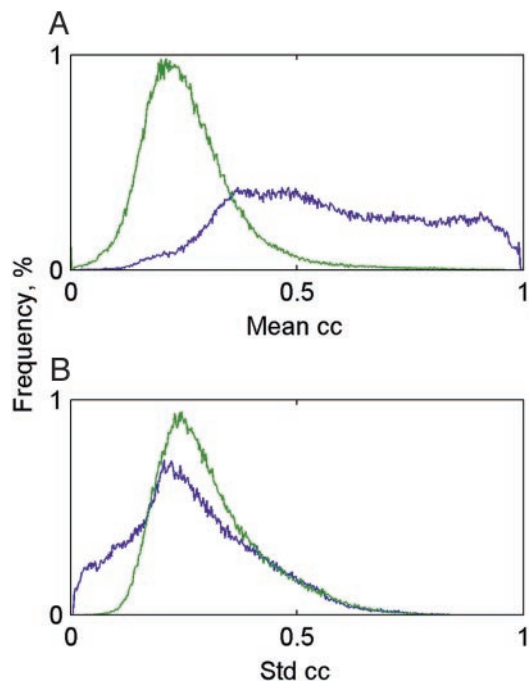


FIG. 3. Histograms of the mean correlation coefficients between partial and full RMFs (A) and their SDs (B). Blue: histograms for data from pixels with significant modulation ($F > 2$), green: histograms of data from pixels with nonsignificant modulation ($F < 2$).

pixels that had significant RMF modulation. There was also a clear, although smaller, shift of the SD toward smaller values (Fig. 3B).

The data presented above suggest that the optical signal is consistently well entrained by the acoustic stimulation in some parts of the cortex. It could still be that the entrainment, although present, may shift its phase slowly over longer periods of the experiment, attributed to changes in the tissue or to effects of previous stimulation periods. To check this, in each experiment one set of parameters was repeated at least twice, with ≥ 2 –5 h between repetitions. Figure 4, A–E show examples of RMFs from pairs of such blocks. Each panel displays RMFs recorded along a line on the cortical surface, chosen to cover a large extent of the significantly modulated area. The *top panel* in each pair corresponds to the data collected in the earlier block and the *bottom panel* to the data collected in the later block. Although there are differences in detail there is a good general agreement in the shape and positions in the RMFs.

The similarity between the RMFs in 2 such blocks was quantified by the correlation coefficient between them on a pixel-by-pixel basis. Any shift in the RMF was quantified by the location of the peak of the cross-correlation function between the RMFs. Figure 4F shows the distribution of the correlation coefficients (purple line) for one pair of blocks (Fig. 4A shows some of these RMFs). The data are shown only for pixels that had significant modulation in both blocks (representing 88% of the pixels in the earlier block and 73% of the pixels in the latter block). The correlation coefficients are generally high, indicating similarity in the shape of the RMFs in the 2 blocks.

Phase shifts in the RMFs between blocks were generally small. Figure 4G shows a histogram of all the shift values, from

all pixels with significant modulation in both blocks (purple) and in the complementary pixels (green). Phase shifts close to 0, indicating the same temporal position of the RMFs in both blocks, were by far the most common, but negative shifts of up to about 3 s were also not uncommon. In contrast, positive time shifts were rarer. Negative shifts indicate a delay of the RMF in the later block relative to the earlier one. Thus it seems that, over time, the RMFs either kept their temporal position or tended to be somewhat delayed in the later block. Examples of such delays are also apparent in Fig. 4, B and C. An average time shift of 1–2 s, over a total stimulus sequence duration of 12 s and about a frequency range of 6 octaves corresponds to a shift in the presumed “trigger frequency” to which the RMF was locked of about 0.5–1 octaves. Because of these limitations in the stability of the RMF over long time periods it is unrealistic to expect the optical data to line up precisely with electrophysiologically determined tonotopic maps that are recorded much later in the same experiment. Misalignments of as much as one octave on average may be expected between the optical and the electrophysiological measurements. However, the shifts in optical trigger frequency themselves were highly correlated across the cortical surface (e.g., Fig. 4, B and C). Thus the large-scale tonotopic organization was nevertheless reflected faithfully in the optical maps.

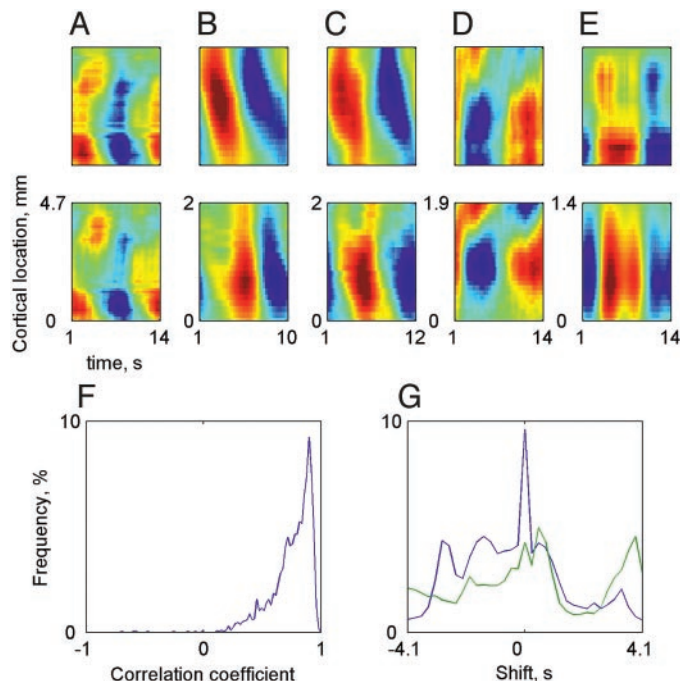


FIG. 4. Stability analysis of RMFs across blocks. A–E: RMFs presented as a function of time along the abscissa and cortical location along the ordinate. Reflectance values are represented by colors. Each pair of panels represent data collected using the same parameters, at the same cortical locations, but with a time difference of a few hours. Data are from 4 of the 5 animals used in this study. Details (animal, color scale saturation of *top panel*, color scale saturation of *bottom panel*): A: F0230, 6%, 5%. B: F0234, 8%, 0.8%. C: F0234, 3%, 0.5%. D: F0242, 2%, 2.5%. E: F0256, 3.7%, 4.5%. F: histograms of the correlation coefficients between the RMFs in corresponding pixels in 2 blocks measured with the same parameters. G: histograms of the time shifts at which the maximum correlation between the RMFs in the 2 blocks was achieved. Purple: histogram for pixels with significant modulation in both blocks. Green: histogram for pixels with nonsignificant modulation in at least one block.

Properties of the RMFs

The RMF, by its construction, has the same period as the stimulation sequence. The RMF can therefore be decomposed into sinusoidal components at the period of the stimulation sequence and its harmonics. Kalatsky and Stryker (2003) argued that at a sufficiently fast stimulation frequency rate, the RMF should be dominated by the fundamental frequency and therefore be roughly sinusoidal. They used the phase of the fundamental as their temporal reference point for the RMF. In our hands, for sequence durations longer than 6 s, the shape of the RMFs was frequently not sinusoidal and depended on the period of the stimulus sequence (Fig. 5A). The asymmetry in the RMFs can be quantified by the relative contributions of the frequency components at the sequence duration (the fundamental H0, with a period of D seconds, where D is the sequence duration) and its 1st harmonic (H1, with a period of D/2) (Fig. 5B). For a sequence duration of 4 s, the first harmonic was on average about 30 dB below the fundamental (amplitude ratio of about 3%), whereas for sequence durations of 10–14 s, at which most of the data were collected, the energy ratio was between –10 and –6 dB, corresponding to amplitude ratios of 30–50%. Thus although the fundamental component was dominant on average, the 1st harmonic (and also higher harmonics) made substantial contributions to the shape of the RMF at the longer sequence durations.

An important consequence of this asymmetry is that the maxima and minima of the RMFs are not good choices for the temporal reference point along the RMF because their location is too dependent on the stimulus sequence duration. This conclusion is illustrated in Fig. 5, C (animal F0230) and D (animal F0256). A set of RMFs, collected along a line on the cortical surface, is displayed. The maxima of the RMFs in Fig. 5C, marked by the black lines, shift very irregularly, whereas the zero crossings show a substantially smoother change (magenta). In Fig. 5D the maxima shift somewhat more regularly, but still less smoothly than the zero crossings. Figure 5E shows an example of a maximum map, and Fig. 5F is a zero-crossing map of one animal (same case as Fig. 5C). The zero crossings do indeed seem to vary in a smoother way across the whole cortical surface.

To quantify this observation, the gradient of the maps was computed at each pixel that showed significant modulation. The gradient was estimated as the vector of differences between each pixel and its neighbors along the x- and y-axes, and the Euclidian length of this vector was used as the magnitude of the gradient. The maxima of the RMFs tended to stay roughly constant and then move in rather large jumps. Therefore the gradient magnitudes of these maps are expected to have an excess of both very small and very large values relative to the gradient magnitudes of the zero-crossing maps. Because zero-crossing maps are smoother, medium gradient values are expected to dominate.

In the data, the gradients had a highly skewed distribution. To compare the gradients of the maxima and of the zero-crossing maps, the average gradient magnitudes and their SDs were computed for each map. The gradients computed for the maxima maps tended to be larger on average ($t = 2.6$, $df = 89$, $P < 0.05$, paired t -test), and more dispersed ($t = 3.4$, $df = 89$, $P < 0.05$, paired t -test), than the gradients computed for the zero-crossing maps. Figure 5G shows a coarse histogram of the

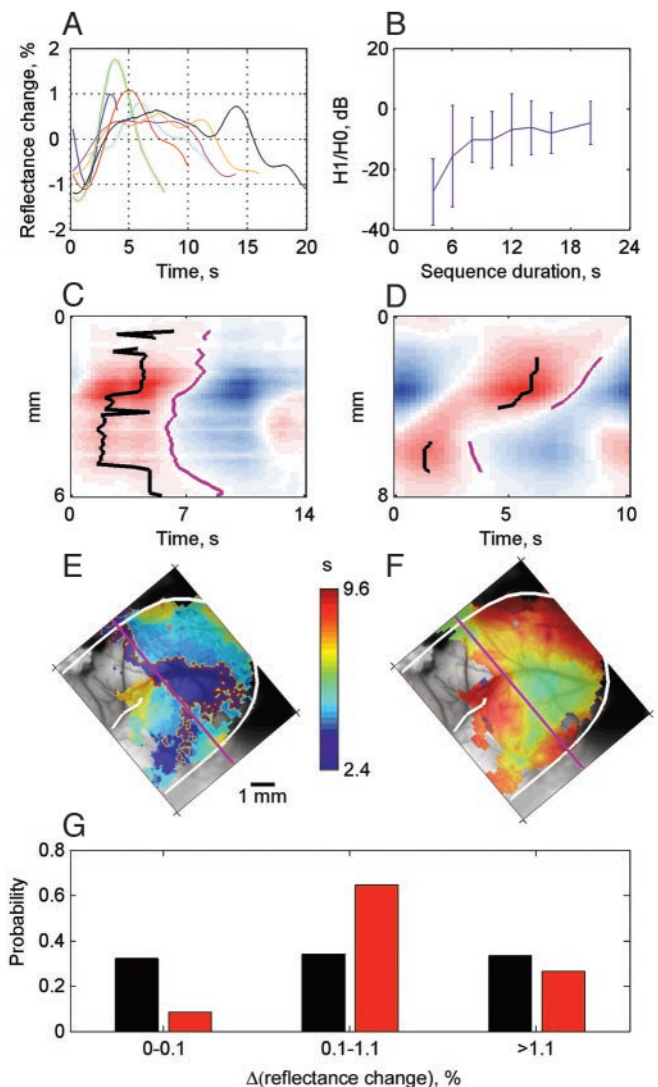


FIG. 5. A: examples of RMFs collected with upward-frequency sequences at the same pixel, but with different stimulus-sequence duration (purple: 4 s; green: 8 s; red: 10 s; cyan: 12 s; magenta: 14 s; orange: 16 s; black: 20 s). Whereas the shape of the RMF is sinusoidal when the sequence duration is 4 s, it becomes much more asymmetric for the longer sequence durations. B: mean and SDs of the ratio between the energy of the first harmonic and the fundamental of the RMFs, expressed in dB. C and D: 2 examples of a set of RMFs collected along a line on the cortical surface (from F0230 and F0256, respectively). Black lines correspond to the locations of the maxima of the RMFs, and the magenta lines to the downward zero crossing. Data are shown only for RMFs with statistically significant modulation ($F > 2$). Color scale in C is clipped at a reflectance change of $\pm 7\%$, in D at $\pm 11\%$. E: map of maxima for animal F0230. F: Map of zero crossings for animal F0230. Magenta line represents the line from which the data in C were extracted. White lines on E and F indicate the location of the suprasylvian and pseudosylvian sulci (see Fig. 1A) for anatomical references. Note the greater smoothness of the zero-crossing map. G: coarse histogram of the gradient magnitudes for maxima maps (black) and zero-crossing maps (red). Zero-crossing maps had an excess of medium gradient magnitudes and a smaller number of small- and large-gradient magnitudes.

2 distributions. The bin widths have been selected to achieve near-uniform counts for the histogram of the gradients computed for the maxima maps (black). In the same bins, the counts for the gradients of the zero-crossing maps (red) were much more concentrated in the second bin, with lower probabilities for both smaller and larger values. These findings fully

justify the use of zero crossings of the RMFs, rather than their maxima, as the temporal reference points.

The fixed-trigger model for the RMFs

To be able to derive estimates of preferred stimulus parameters from the RMF it is necessary to estimate the temporal relationship between the RMF and the start of the stimulus sequence. In the example shown in Fig. 1 the start of the stimulus sequence happened to coincide with a minimum in the RMF, but that was not always the case: for other pixels or stimulus conditions the temporal relationship between the RMF and the sequence onset was quite different, as seen in Fig. 2. Our data analysis is based on the assumption that the RMF is the signature of a stereotyped response of a cortical pixel, which is “triggered” when the stimulus sequence crosses the tuning curves of the neurons in the pixel. Consequently, if we understand the (presumably fixed) temporal relationship between an identifiable reference point on the RMF (e.g., the downward zero crossing) and the “trigger point,” then we can deduce which stimulus parameter triggered the response. The slow time course of the optical signal implies that the analysis method presented here cannot be used to deduce the “selectivity” of the optical signal recorded from a given pixel to the stimulus parameter, given that it is very difficult to relate the time course of the signal following the trigger point to the properties of the stimulus sequence. Instead, we identify here the “sensitivity” of the optical signal to the stimulus parameter, as indicated by the parameter value that caused the triggering of the optical response. Hereafter, this parameter value will be called the *trigger parameter*.

In the simplest version of this model, the “temporal position” of the RMF relative to the start of the stimulus sequence is determined by 2 factors. One is a fixed delay T, which depends on the dynamics of the reflectance signal, and is expected to be on the order of a second or so (Devor et al. 2003; Martindale et al. 2003; Nemoto et al. 2004). This delay could, in principle, also depend on the total latency between sound presentation and the response of the cortical neurons. However, neuronal response latencies, on the order of a few tens of milliseconds, are substantially shorter than the latency because of the dynamics of the reflectance signal itself and can therefore be ignored. The second factor determining the temporal position of the RMF is the time from the beginning of the sequence until the trigger parameter value. If we take downward zero crossings as points of reference on the RMF, then these temporal relationships are given by the following equation (see Fig. 6 for schematic representation)

$$zc(x, y) = T + \frac{freq(x, y) - freq(start)}{freq(end) - freq(start)} D \quad (1)$$

where $zc(x, y)$ is the time of the zero crossing at the pixel with coordinates x and y ; T is the delay, assumed to be fixed across conditions and across the imaged area; $freq(x, y)$ is the parameter value that triggers the response; and D is the duration of the sequence that starts at parameter value $freq(start)$ and ends at parameter value $freq(end)$. Note that $freq(start)$, $freq(end)$, D , and $zc(x, y)$ are either set by the experimenter or easily measured. We sought to determine $freq(x, y)$, but to do so we also need to estimate the unknown delay T .

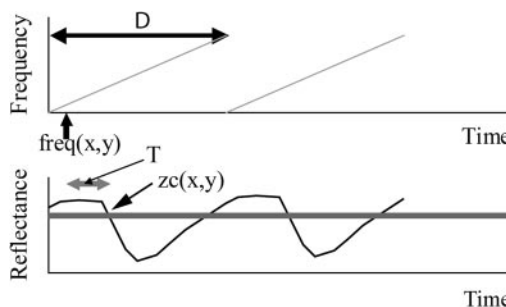


FIG. 6. Illustration of the fixed-trigger model. *Top panel:* representation of the stimulus sequence. *Bottom panel:* optical signal. According to the fixed-trigger model, whenever a trigger frequency $freq(x, y)$ occurs, the change in the optical signal is triggered after a delay T , which is independent of the cortical location.

In principle, the delay can be extracted by measuring $zc(x, y)$ for 2 or more stimulus conditions, such as data collected with 2 sequence durations or data from an upward- and a downward-frequency sequence. A factor complicating this solution is phase ambiguity. For example, a zero crossing occurring just after the beginning of a stimulus sequence could be triggered by the occurrence of a stimulus parameter at the end of the preceding repeat of that sequence.

The simple “trigger parameter” model described here is, of course, likely to be an oversimplification. In the data described below, it is clear that either the delay or the trigger frequency (and probably both) depend on the exact stimulation paradigm used (ascending vs. descending frequencies, sequence duration, and so on). Consequently, the tests of the trigger model described below are unlikely to be borne out with precision, but insofar as they yield at least approximately correct results they do lend support to the validity of the derived estimates of sensitive (“trigger”) parameter values.

The fixed-trigger model: sequences of varying durations

One way of verifying the suitability of the model is by comparing the results of measurements with different stimulus sequence durations. Assuming that $freq(x, y)$ is independent of duration, it is easily shown that

$$\frac{zc(x, y, D1)}{D1} = \frac{zc(x, y, D2)}{D2} + T \left(\frac{1}{D1} + \frac{1}{D2} \right) + k \quad (2)$$

where k can have integer values because of phase ambiguities. Thus the zero crossings at 2 different durations, normalized by the appropriate sequence duration, should be linearly related except for a constant shift. Furthermore, a plot of $zc(x, y)$ as a function of sequence duration D should produce a straight line, from which, in principle, T and $freq(x, y)$ can be determined. As expected, these predictions based on the simple trigger model were not borne out precisely, but they did yield reasonable approximations in many of the cases.

Figure 7 shows the results of these tests carried out with data collected at different sequence durations. Figure 7, *A* and *B* show RMFs collected in pixels along a line on the cortical surface, for sequence durations of 6 and 10 s (animal F0256). The zero crossings consist of 2 segments interrupted by some pixels with nonsignificant modulation. Figure 7*C* is a plot of the zero crossings, divided by the duration of each sequence as in Eq. 2; the zero crossings for the other sequence duration

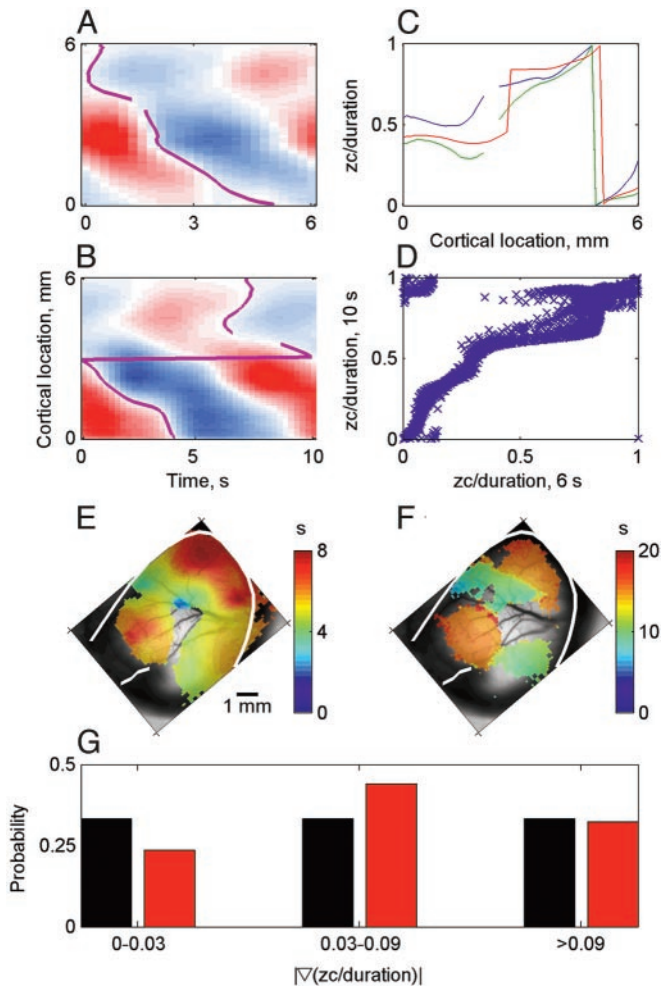


FIG. 7. *A* and *B*: RMFs collected along a line on the cortical surface from animal F0256. Color-scale saturation at 5% (*A*) and 15% (*B*). *C*: zero crossings, normalized by the duration of the sequence, for 3 durations: 6 s (purple) and 10 s (green), from the full data in *A* and *B*, and 14 s (red, full RMFs not shown). Zero crossings were shifted by 3.4 s (14 samples). *D*: scatter plot of the zero crossings for the 6- and 10-s data, for all cortical locations that had significant RMFs at both durations. Note the approximately linear relationship with a slope close to 1 between the two. *E*: zero-crossing map for a sequence of 10 s (animal F0234). *F*: zero-crossing map for the same animal as *E*, for a sequence of 20 s. Note the large patches of almost constant zero-crossing value in *F*. White lines on *E* and *F* indicate the location of the suprasylvian and pseudosylvian sulci (see Fig. 1*A*) for anatomical references. *G*: coarse histogram of normalized zero-crossing gradients for short sequences (durations <14 s, red) and for long sequences (durations >14 s, black).

tested in this animal, 14 s, are also displayed. The zero crossings have been referred backward by 3.4 s (14 samples), to position the phase jump at approximately the same location for the data at all 3 sequence durations. In this plot, the 3 lines should be parallel to each other (their distance being determined by the delay, see Eq. 2). The data in Fig. 7*C* are roughly, though not precisely, consistent with this prediction. Figure 7*D* displays the scatter plot of the zero-crossing times at the 2 shorter durations (6 and 10 s), normalized by the duration (as in Eq. 2) and corrected for phase ambiguity, at all pixels in which the RMFs had significant modulation for both sequences. The scatter plot showed a roughly monotonic relationship between $zc(x, y)$ and D , with a correlation coefficient of 0.84. Correlation coefficients were computed for 40 pairs of maps measured with different durations. The average correla-

tion coefficient was 0.75 ± 0.13 (mean \pm SD), and thus the example in Fig. 7*D*, although somewhat above average, is typical.

The main departure of the data in Fig. 7, *C* and *D* from the prediction of the fixed-trigger model is the staircase shape—the zero-crossing values derived from the 10 s sequence tended to change in jumps relative to those of the 6-s sequence (Fig. 7*D*), and the staircase shape is even stronger for the 14-s sequence (Fig. 7*C*; compare the red line with the other two). This example illustrates the general tendency of the zero crossings for the sequences of longer durations to contain relatively large areas of constant values, interrupted by sharp discontinuities. At the same locations, sequences of shorter durations could give rise to smoother transitions. This phenomenon is illustrated again in Fig. 7, *E* and *F*, showing the zero-crossing maps for upward-frequency sequences of 10 and 20 s duration, respectively (animal F0234). The general structure of the two zero-crossing maps is comparable, with 2 clusters of relatively late values, one dorsal and posterior and the other one more anterior and ventral, separated by a region of earlier zero crossings. However, whereas the changes in zero crossings in the map extracted from the 10-s sequence (Fig. 7*E*) are gradual, they occur in sudden jumps for the map extracted from the 20-s sequence (Fig. 7*F*).

We examined this quantitatively using the gradients of the zero-crossing maps. For maps that contain regions of constant values interrupted by discontinuities, as in Fig. 7*F*, it is expected that the magnitude of the gradients will show an excess of both small and large values, whereas maps with smoother variation would show mainly intermediate gradient magnitudes. Figure 7*G* shows a coarse histogram of the gradient magnitudes. The gradient magnitudes, computed for all bins with significant modulation of the RMF, have been separately collected for maps generated with frequency sequences of durations shorter and longer than 14 s, respectively. The bins in Fig. 7*G* have been selected to give equal counts in the histogram of the gradient magnitudes for the maps computed with long durations (black). Using these bins, there is clearly an overrepresentation of intermediate gradient magnitudes in the maps computed for shorter durations (red), confirming the presence of smoother changes in the zero-crossing values across the cortical surface at those durations.

The fixed-trigger model: upward versus downward sequences

Another way of testing the fixed-trigger model is by comparing responses to upward- and downward-frequency sequences (Kalatsky and Stryker 2003). In these cases, the fixed-trigger model predicts that

$$zc(x, y; \text{up}) + zc(x, y; \text{down}) = 2T + kD \tag{3}$$

where k can have integer values as a result of phase ambiguities. It is expected therefore that the values of $zc(x, y; \text{up})$ and $zc(x, y; \text{down})$, after unwrapping of phase ambiguities, will be inversely related to each other: when one of them increases, the other should decrease with a slope of -1 . Intuitively, this is obvious, given that an increase in zero-crossing time for an upward sequence signifies a higher trigger frequency, corresponding to a decrease in the zero-crossing time for a downward sequence.

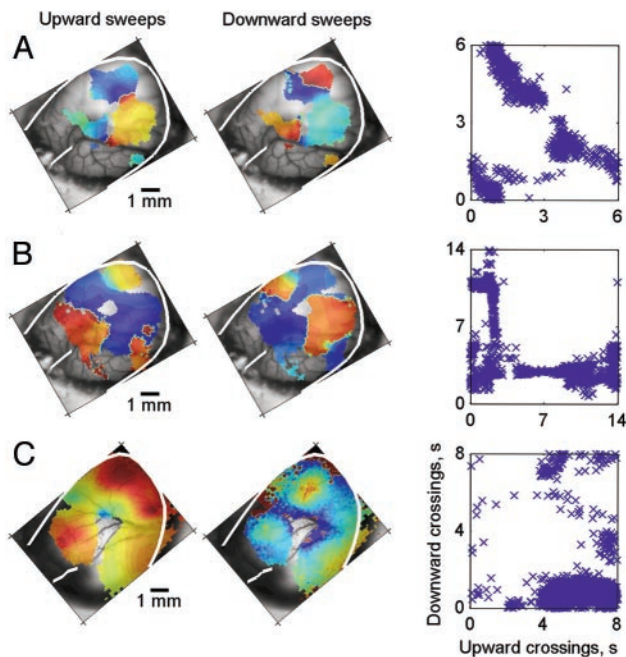


FIG. 8. *A*: pair of zero-crossing maps for upward- and downward-frequency sequences from animal F0242, and the resulting scatter plot. White lines in these and the other parts of this figure indicate the location of the suprasylvian and pseudosylvian sulci (see Fig. 1*A*) for anatomical references. This pair of blocks showed the expected linear relationship between the zero crossings of upward and downward sequences, with a slope of -1 . Color map is saturated at 0 and 6 s (the sequence duration). *B*: similar data for another pair of blocks in the same animal. In this case, in spite of the negative correlation between the 2, a linear relationship is not seen. Sequence duration was 14 s. *C*: similar data for another animal (F0234). Two maps are positively correlated when no delay is applied. With the appropriate pair of delays, a negative, although weak, correlation is found ($r = -0.12$, see text). Sequence duration was 8 s.

To quantify the general relationships between the zero-crossing times for the upward- and downward-frequency sequences, the correlation coefficients between them were calculated for all such pairs of maps. Because phase wrapping could affect the quality of the fit, the maps were shifted cyclically by all possible values, and the best (most negative) correlation coefficient was determined. Figure 8 shows 3 examples of such scatter plots. Figure 8*A* is the best case in the whole data set. The inverse relationship is clearly apparent, in that regions of early zero crossings in one map correspond to regions of late zero crossings in the other map, and the slope of the scatter plot is approximately -1 . However, only 2 map pairs out of 10 tested, both from the same animal (F0242), showed this type of behavior.

Figure 8*B* is a more typical example. Although the correlation coefficient between the zero-crossing times in the 2 maps is negative, it is clear that the relationships between the zero-crossing maps are not simple. In a rough way, regions of early zero crossings in the map derived from the upward-frequency sequences correspond to regions of late zero crossings in the map derived from the downward-frequency sequences. However, the relationship is far from the linear one expected from the fixed-trigger model, and there are regions in which this relationship does not hold. Figure 8*C* shows an extreme example—here the upward and downward zero crossings seem to be positively correlated, rather than negatively correlated. Because all possible shifts of the 2 maps were

tested, the best correlation coefficient is still negative, although small in absolute value.

Ten pairs of maps were compared with this approach. Best-correlation coefficients varied between -0.8 (the data shown in Fig. 8*A*) to -0.12 (the data shown in Fig. 8*C*). The mean correlation coefficient was $-0.42 (\pm 0.23 \text{ SD})$. The data in Fig. 8*B* had a correlation coefficient of -0.51 , and are therefore typical.

Tonotopic maps

To compute maps of trigger parameters from the RMFs at each pixel, the temporal reference point on the RMF was determined as the lag corresponding to the downward zero crossing of the RMF. This choice is justified by the data presented in Fig. 5. Furthermore, in all animals except one (F0242), only upward-frequency sequences were used because of the general incompatibility between the upward and downward maps, as shown in Fig. 8. Animal F0242 was exceptional in that it was the only one with reasonably compatible upward and downward zero-crossing maps (Fig. 8*A*). Both of these choices are different from those made by Kalatsky and Stryker (2003), but are justified by the character of the data as described above.

Using the data collected with a variety of pure-tone sequences, trigger-frequency maps were created for each possible value of the delay T . For each value of T , the similarity between the maps from all pure-tone sequences was estimated by computing their variance around the mean, averaged over all pixels that had significantly modulated RMFs in at least 2 conditions. The delay T that corresponded to the least-variable map was selected. This procedure is similar to linear regression of the zero-crossing times against stimulus duration, but with the intercept fixed across all pixels and with weighting that emphasizes the shorter sequences. The emphasis of the shorter sequences is justified by the data presented in Fig. 7.

This procedure is illustrated in Fig. 9. The data for sequence durations of 8 and 16 s, collected in the same animal (F0234), are shown in Fig. 9, *A* and *B*, at a delay of 1.7 s (the best delay for this data set). The consensus map, based on all the available

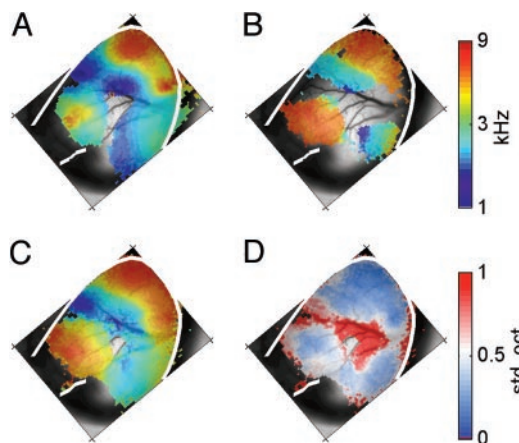


FIG. 9. Frequency maps derived from upward-frequency sequences. *A* and *B*: frequency maps from 8- and 16-s upward tone sequences from the same animal (F0234). Delay used was 1.7 s (7 samples). *C*: consensus map for the same animal as in *A* and *B*. For this animal, 7 durations were used: 4, 8, 10, 12, 14, 16, and 20 s. *D*: SD of the log(frequency) estimates in each pixel of *C*, expressed in octaves.

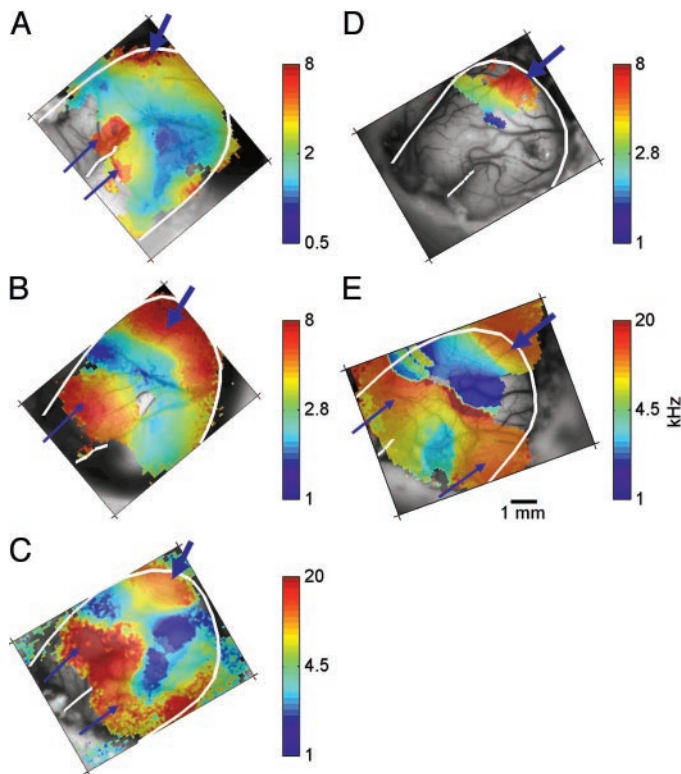


FIG. 10. Frequency maps for the 5 animals. *A*: animal F0230. Delay: 0.48 s. *B*: animal F0234. Delay: 1.7 s. *C*: animal F0242. Delay: 0.24 s. In this animal, both upward- and downward-frequency sequences were used to derive the frequency map (see text for more details). *D*: animal F0253. Delay: 1.96 s. *E*: animal F0256. Delay: 0.72 s. Thick blue arrows point to the postero-dorsal high-frequency area, corresponding to high-frequency A1/AAF. Thin blue arrows point to the ventral high-frequency areas on the AEG and PEG.

data for this animal (durations of 4, 8, 10, 12, 14, 16, and 20 s), is shown in Fig. 9C, and Fig. 9D shows the SDs in the frequency estimates at each pixel. The data are shown only for pixels where at least 2 valid estimates of the zero crossings ($F > 2$, as derived from the ANOVA) were available. The maps were not spatially smoothed in any way. The maps estimated from single-sequence durations are rather similar to each other, and this is expressed in the relatively low SD of the frequency estimates over most of the cortical surface (<0.5 octaves in 56% of the pixels, and larger than one octave in only 16% of the pixels).

The frequency maps for the 5 animals are displayed in Fig. 10. The delays used are displayed in the figure legend, and ranged from 0.24 to 1.92 s. It should be emphasized that the delay, by itself, fixes the absolute scale of the map but not its structure. The location of the frequency gradients and reversals should not be affected by a small change in the delay. Furthermore, for the rather long sequences used here (typically 14 s), a change of 1 s in the delay represents less than half an octave in frequency sensitivity. This is the same order of magnitude of other uncertainties in the generation of the frequency map (e.g., Fig. 4).

Although the maps in Fig. 10 illustrate marked variability between individual animals, they also reveal a number of common features (to be described more fully below). To support the physiological validity of these maps, standard tone maps were collected using the paradigm developed by Versnel et al. (2002) for 3 animals (F0230, F0234, and F0242). These

maps were smoothed as described in the METHODS and are displayed in Fig. 11. The differences between the maps derived from the tone sequences, and the maps derived from the standard stimulation paradigm are much smaller than the variability between the maps measured in different animals.

Thus the maps of animal F0230 (Figs. 10A and 11, A and D) show a preponderance of low-frequency sensitivity. In Fig. 10A, this low-frequency dominance is expressed as relatively early zero crossings, whereas in Fig. 11D it is expressed by the much larger areas whose responses were dominated by the low frequencies than by the high frequencies. The maps of animal F0234 (Figs. 10B and 11, B and E) show a central low-frequency area with high-frequency areas both posterodorsally and anteroventrally. The main difference between these maps is on the PEG, posterior to the pseudosylvian sulcus. In Fig. 10B this area shows low-frequency sensitivity, whereas in Fig. 11, B and E the corresponding area shows high-frequency responses. This is attributed to the fact that this region was not activated at all by the low-frequency tones used in the standard stimulation paradigm. However, over most of their common range, the 2 maps are similar. Finally, the maps of animal F0242 (Figs. 10C and 11, C and F) again show a strong similarity, including the medium-frequency “ridge” connecting the dorsal and the ventral high-frequency areas and separating 2 areas of lower-frequency sensitivity.

Generally, the frequencies assigned to each pixel using the standard paradigm of presenting one tone frequency at a time

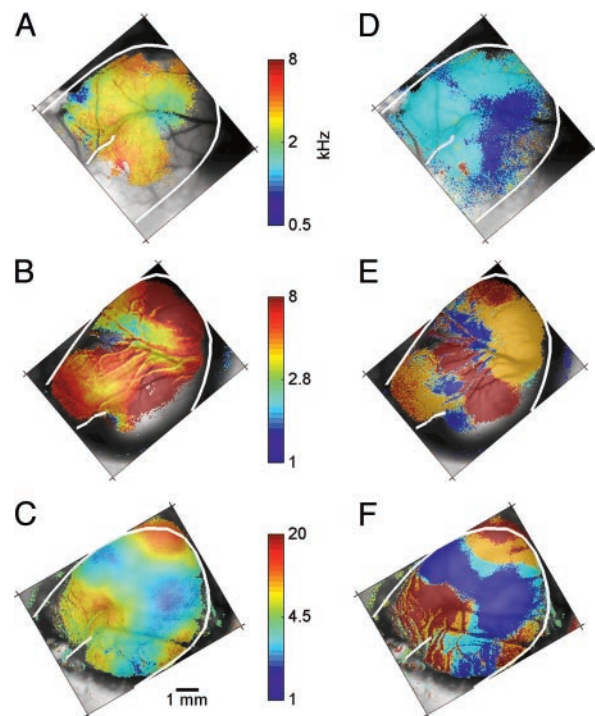


FIG. 11. Frequency maps derived by imaging intrinsic signals evoked by tone pip trains with different center frequencies for the 3 animals in which these data were collected. *A* and *D*: animal F0230. Scale corresponds to the scale used for this animal in Fig. 11A. In *D*, the sensitivity map is presented as in Versnel et al. (2002). Each pixel is colored by the index of the frequency that gave rise to the largest signal (blue: 1 kHz; cyan: 2.8 kHz; orange: 8 kHz; red: 16 kHz). In *A*, the same data are smoothed by averaging the frequencies that activated each pixel, weighted by their activation level. *B* and *E*: animal F0234. Same conventions as above. *C* and *F*: animal F0242. Same conventions as above.

(Fig. 11) are higher than those assigned using the frequency sequences (Fig. 10). This difference may be attributable to the use of upward sequences for estimating the trigger frequencies. Using such sequences, it is expected that the neurons will be activated when the sequence enters their sensitive areas from below, at frequencies that are below the BF. This would be true even in the presence of lower inhibitory sidebands, given that metabolic demand, which determines blood flow, is thought to depend on the total synaptic activity rather than on the spiking activity (Logothetis et al. 2001).

Large-scale organization of the tonotopic map

The tonotopic arrangement in ferret auditory cortex based on the optical maps (Fig. 10) consists of a central low-frequency area with flanking high-frequency regions. In all maps, a high-frequency focus was found in the dorsal part of the MEG (see Fig. 1A, marked with thick arrows in Fig. 10). In 4 animals, additional high-frequency areas (marked with thin arrows in Fig. 10, A–C and E) were also found ventral to the low-frequency central area. The high-frequency focus located at the dorsal part of the MEG (thick arrows) most likely corresponds to the high-frequency end of areas A1 and AAF. A frequency gradient extending ventrally from the tip of the MEG is consistent with the A1 frequency gradient as usually defined in the ferret, and was seen in all animals. In no case, did we observe a clear frequency reversal within this high-frequency area that could be interpreted as a border between high-frequency A1 and AAF. In addition, except for one animal, we did not observe any clear discontinuity within the central low-frequency region that could be interpreted as the border between low-frequency A1 and AAF (as in Fig. 10, A, B, and E). In one case (Fig. 10C, animal F0242), a middle-frequency ridge was present that could indicate the border between the low-frequency A1 and AAF regions. Such a region has also been observed in tonotopic maps generated using electrophysiological recordings (e.g., Kelly et al. 1986) and was also seen in the map generated from the standard simulation paradigm in this animal (Fig. 11C). Thus in terms of tonotopic organization, A1 and AAF appear to share a continuous gradient that runs approximately dorsoventrally from the MEG to the PEG and AEG, respectively.

Beyond the A1/AAF area, the optical maps consistently showed a frequency reversal and high-frequency sensitivity on the AEG, PEG, or both (Fig. 10, A, B, C, and E). The only exception is one animal (F0253, Fig. 10D) in which the RMFs in response to tone sequences outside A1/AAF were not significant. The observed frequency reversals are indicative of borders with additional, presumably higher-order, auditory fields. Thus our studies reveal at least 2 new fields: one on the AEG, ventral to A1 and AAF and anterior of the pseudosylvian sulcus, and another on the PEG ventral to the primary fields and posterior to the pseudosylvian sulcus. There may be additional fields between these two, lying inside the pseudosylvian sulcus itself, but such fields cannot be visualized with optical signals.

Single-unit recording data (Phillips et al. 1994) suggest that the representation of sound frequency in A1 may break down at high sound levels. However, in keeping with other imaging studies (Harrison et al. 1998; Spitzer et al. 2001; Versnel et al. 2002), we found that the frequency gradients in A1 and AAF

were preserved at high levels, and that the RMFs remained significantly modulated by acoustic stimulus parameters. Because the optical signals are thought to reflect synaptic activity rather than the spiking output of the cortex (Nemoto et al. 2004), this finding may imply that the patchiness observed in the electrophysiological tone-frequency maps is a result of cortical processing of inputs that have a much stricter tonotopic order, even at high sound levels.

Relationship between optical and electrophysiological data

To compare the frequency maps derived from the RMFs with electrophysiological measures of neural tuning, a small number of microelectrode recordings were performed in each animal after the optical recordings had been completed. The responses of 63 multiunit clusters were recorded, of which 53 were recorded at locations to which a frequency could be assigned based on the optical recordings; for 48 of these clusters, a best frequency could be assigned to the electrophysiological data. The responses of the other 5 clusters were not tuned for frequency.

Figure 12 shows examples of frequency response areas derived from the electrophysiological recordings. Three types of behavior can be distinguished. In 15/48 cases, the best frequency of the cluster and the optical frequency were less than half an octave apart. Examples for these cases are shown in Fig. 12, A and B. These cases were about twice as likely to occur inside A1/AAF (11/15) as outside A1/AAF (4/15).

The second type of behavior is illustrated in Fig. 12, C and D. In these cases (21/48 multiunit recordings), the optical frequency was more than half an octave lower than the cluster BF, and occurred within the low-frequency tail of the frequency response area. This is presumably attributable to the fact that the upward sequences were used to estimate the

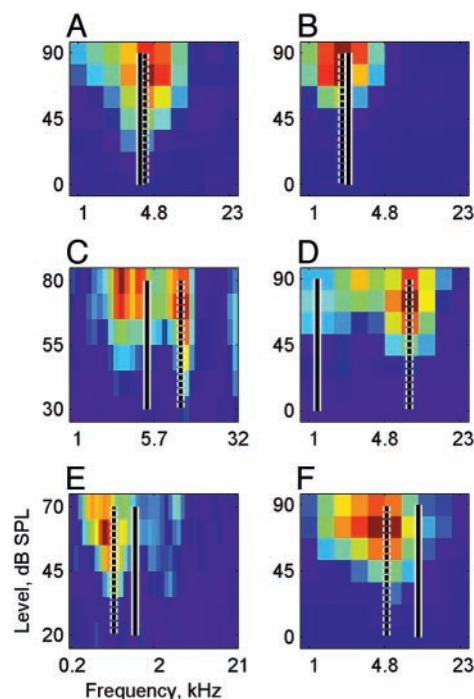


FIG. 12. Frequency response planes of multiunit clusters. Dashed line is the estimated best frequency (BF) from the cluster responses, and the continuous line is the estimated BF from the optical recording at the electrode position.

tonotopic maps and, for these sequences, the trigger point for the optical signal occurred when the frequency entered the sensitive region of the unit's tuning curve below the BF. These cases were less common in A1/AAF (7/21 units) than outside A1/AAF (14/21 units).

Finally, in the third type of clusters, the optical frequency was located more than half an octave above the cluster BF (12/48). These included all 8 clusters with BFs < 2 kHz (Fig. 12E). At these low BFs, the optical frequency estimates may be distorted because of the large frequency jump that occurred in the stimulus sequence between the very high frequencies at the end of one repeat of the sequence and the very low frequencies at the beginning of the next repeat. Of the remaining 4 clusters with this behavior (4/48, Fig. 12F), 2 occurred within A1/AAF and the other 2 outside A1/AAF.

All the examples in Fig. 12, except that in Fig. 12C, are from A1/AAF. The recording location of Fig. 12C was at the high-frequency anterior area of F0230, just dorsal to the tip of the pseudosylvian sulcus (Fig. 10A).

The distributions of the different classes inside and outside A1/AAF were not statistically different ($\chi^2 = 5.6$, $df = 2$, ns).

To verify that the relationship between cluster BFs and optical frequencies was not random, we assumed a model in which the BFs estimated from the electrophysiological recordings are given, and the optical frequencies are randomly distributed across the cortical surface. In this model, it is possible to estimate the probability of finding an optical frequency within a given interval from a cluster BF simply as the ratio of the length of this interval and the frequency range spanned by the stimulus sequence. Using this approach, the expected number of penetrations for which the optical frequencies would be within half an octave from the BF was 8.3, whereas the actual number of cases, 15, was significantly higher ($\chi^2 = 10.5$, $df = 1$, $P < 0.01$). So although BFs and optical trigger frequencies often differed by more than half an octave, their relationship was much closer than would be expected by chance.

DISCUSSION

We used optical imaging of intrinsic signals to study the large-scale organization of ferret auditory cortex. In addition to frequency gradients consistent with the known organization of ferret A1 and AAF on the MEG, we observed new, as yet largely uncharted, acoustically responsive areas on the AEG and the PEG. These areas correspond to the pattern of sound-evoked 2-deoxyglucose uptake reported by Wallace et al. (1997) and suggest that ferret auditory cortex is composed of at least 4 and probably more areas.

The use of continuous sequences is new, and results using this method have been published until now only in the rat visual cortex (Kalatsky and Stryker 2003). Thus in this study, we carried out a detailed examination of the properties of the optical signal evoked during continuous stimulation and its relationships to the parameters of the stimulation sequence. We will discuss here 1) the validity of the fixed-trigger model; 2) optimal sets of stimulation parameters for generating the optical maps; and 3) the validity of the resulting frequency maps.

The fixed-trigger model

The interpretation of the data collected with continuous-sequence stimulation assumes that the optical signal is generated when a stimulus-frequency sequence crosses some trigger value, which is representative of the frequency selectivity of the neural elements in the tissue. The optical signal and the crossing of the trigger frequency are thought to be separated by an unknown but constant delay. Finding this constant delay is important for fixing the scale, but not the shape, of the frequency map.

Our results show that the fixed-trigger model is at best only an approximation, and that this approximation may hold sufficiently well over only a narrow range of parameters. Two main departures from the fixed-trigger model are documented here. The first is the change in the structure of zero-crossing maps at long-sequence durations, when the maps lose their smoothness and become a mosaic of regions of rather fixed values (Fig. 7). The second, and much larger, departure from the fixed-trigger model is the general lack of concordance between the zero-crossing maps derived from upward- and downward-frequency sequences (Fig. 8).

The partial failures of the fixed-trigger model could result from both sensory and nonsensory factors that contribute to the generation of the optical signal. It has been shown a number of times (e.g., Heil et al. 1992; Nelken and Versnel 2000) that frequency-modulated sweeps produce responses when they cross the border of the tuning curve. In many cases, the response can be shown to be triggered at a frequency that is independent of the velocity of the sweep, with the trigger frequency below the best frequency for upward sweeps and above the best frequency for downward sweeps. A similar phenomenon could occur here, producing different zero-crossing maps for frequency sequences of opposite directions.

More generally, a large number of studies have shown that the responses of neurons in A1 depend on their stimulation history (e.g., Brosch and Schreiner 1997; Calford and Semple 1995; Malone et al. 2002; Ulanovsky et al. 2003). It could be that other adaptive mechanisms, specific to the type of frequency sequences that we used, are responsible for the large differences between the results from the upward and downward sequences. Such adaptation could also affect the results of optical imaging of more complex parameters, and the resulting maps could reflect the interplay of pure sensory responses with specific adaptation mechanisms.

However, under this scenario, it would still be expected that the maps derived from upward- and downward-frequency sequences would show negative correlation. Furthermore, even in the cortex, the high-frequency borders of auditory tuning curves tend to be steeper than the low-frequency borders (e.g., Fig. 12). Consequently, it would be expected that downward-frequency sequences would produce more consistent and representative zero-crossing maps than upward sequences. Instead, the more consistent maps were produced using upward sequences.

Furthermore, these arguments fail to explain the remarkable similarity between the frequency maps determined using the upward sequences and the maps based on the standard, single-tone stimulation paradigm (Figs. 10 and 11). Existing information about the differences in cortical responses to upward and downward chirps in ferret cortex, the closest stimuli to the

tone sequences used here, does not support such large differences between the responses to upward- and downward-frequency sequences (e.g., Nelken and Versnel 2000; Shamma et al. 1993).

A different, complementary explanation for the differences between the optical signals produced by upward- and downward-frequency sequences is the possibility of interactions between the hemodynamical changes produced by the stimulus and nonsensory, dynamical constraints ascribed to general properties of the blood supply to the brain tissue. At the shorter wavelengths used here to image the cortex, the optical signal is thought to reflect mostly changes in blood volume (Frostig et al. 1990). It has long been known (Berne and Levy 1993; p. 483) that the local metabolic state governs blood supply through a number of feedback mechanisms. Harrison et al. (2002) described the presence in auditory cortex of arterioles, with thick smooth muscle layers, which have precapillary sphincters, rings of smooth muscle, at the points where the capillaries branch. The contraction of these muscles is presumably involved, in response to metabolic and other factors, in the fine control of blood flow to the capillary beds and therefore in the origin of the measured optical signal (Harrison et al. 2002). Such metabolic control on blood flow would consist of a negative feedback loop with time constants of a few seconds (as judged for example from the vasomotion signal; Mayhew et al. 1996). This dynamical system would be driven by the stimulus sequence, which determines the sequential changes in the activity of the tissue. We hypothesize that the architecture of the vasculature and the internal dynamics of the blood flow interact with the external dynamics imposed by the continuous sequence to generate the optical signal.

In the ferret, the blood supply to the ectosylvian gyrus arrives and leaves the tissue in large vessels that are oriented roughly along isofrequency contours. Small vessels branch orthogonally, following the frequency gradients. Such an arrangement is clearly seen for example in Fig. 10, *A*, *B*, and *E*. The sequence of volume changes imposed by the direction of the frequency sequence would occur in one direction along this network for upward-frequency sequences, and in the other direction for downward-frequency sequences. Given the directed character of blood flow, from arteries to veins, it is conceivable that such changes interact differently with the underlying dynamics of blood flow. The nature of these interactions is difficult to predict, given that it depends on numerous interdependent and time-varying factors, but it is certainly conceivable that "asymmetries" in these interactions are largely responsible for the significant differences between the zero-crossing maps derived for upward- and downward-frequency sequences.

Although these are mostly speculations, the results presented here strongly suggest that the relationships between the optical signal and the underlying neural activity are not attributed to sensory factors only. They are related to each other through the action of the complex dynamic system that controls blood flow through the cortical tissue. The measured optical signal is therefore the combined result of the external dynamics imposed by the stimulation sequence and the internal dynamics attributed to the blood flow.

Parameter ranges for estimating frequency maps

Kalatsky and Stryker (2003) suggested using sequences of opposite directions to estimate and compensate for the fixed delay, but their argument depends very strongly on the assumption that the delay is indeed constant and independent of whether stimulus sequences move up or down. Our results imply that this approach of using sequences of opposite directions, although successful in early visual cortex, cannot be used in general in auditory cortex. Instead, the constant delay should be estimated by using sequences of the same direction but with different durations.

In this study, most data were collected with stimulus sequence durations of 12 or 14 s, which are just at the border of being too long, as judged from the smoothness of the zero-crossing maps. Improved estimates of cortical sensitivity to sound frequency could, in principle, be made by using shorter-sequence durations.

However, there are two problems with using shorter sequences. First, in 2 of the 5 ferrets, vasomotion artifacts (Mayhew et al. 1996) were observed, with a period of about 8 s. Because the vasomotion is both highly periodic and, when present, the dominant optical signal, sequence durations of about 8 s cannot be used. The useful range is therefore 10–14 s as used here, or ≤ 6 s.

The second problem with using short sequences stems from the slow intrinsic dynamics of the optical signal. The "impulse response" of the optical signal, at the green wavelength, is about 5 s long (our unpublished observations; see also Martindale et al. 2003 for explicit measurements of the volume impulse response). Thus the optical signal would not be able to follow sequences much shorter than 6 s.

In summary, useful data can be collected under these conditions only with sequence durations of 4–6 s and of 10–14 s. In our hands, data collected at 3 durations were sufficient to generate reasonably consistent maps, and therefore durations of 4, 6, and 10 s are probably the best choice for further work.

Validity of the frequency maps

In spite of the various complications described above there are a number of factors that confirm that the maps we generated are representative of the large-scale tonotopic order of ferret auditory cortex.

First, the optical signals were locked to the sensory stimuli in a significant way and therefore represented true indications of tissue activation resulting from the sensory stimuli. The stability of most recordings within a block (Fig. 2), their reproducibility across blocks (Fig. 3), and the rough agreement with the fixed-trigger model all validate their use as indicators of tissue frequency sensitivity.

Second, in all 3 animals examined, the maps derived from the tone sequences and those derived using a standard stimulation paradigm, in which the intrinsic signals were measured in response to repeated presentation of a single stimulus (Versnel et al. 2002), were in good agreement with each other (Figs. 10 and 11). Thus the 2 stimulation paradigms provide generally consistent results.

Third, there is a general, although not exact, agreement between the optically derived trigger frequencies and the BFs of multiunit clusters recorded at the same locations (Fig. 12). It

should be emphasized that the electrophysiological recordings were done once the imaging was complete and there may be some imprecision in the determination of the recorded locations. Furthermore, as seen above, the optical data were stable only up to about an octave over the duration of the experiment. In spite of these sources of variation, optically derived trigger frequencies were generally found to be at, or below, the multiunit BF. This is consistent with the use of upward sequences that may activate a given neural tissue through the low-frequency tail of the tuning curves of the neurons.

Fourth, the structure of the optical maps is generally consistent with the structure of maps derived from electrophysiological recordings where such maps are available, that is in A1 and AAF (Kelly and Judge 1994; Kowalski et al. 1995; Phillips et al. 1988). In particular, the expected dorsoventral frequency gradient over the posterior part of the MEG was present in all maps. This gradient is also consistent with the frequency gradient demonstrated using optical techniques in the same region by Versnel et al. (2002).

Large-scale tonotopic organization of ferret auditory cortex

Ferret auditory cortex consists of a low-frequency area at the center of the MEG, with areas of higher-frequency sensitivity surrounding it. A frequency gradient oriented toward the tip of the gyrus is consistent with the tonotopic gradient demonstrated electrophysiologically in A1 and AAF. In most cases, we did not observe a frequency reversal that could indicate an A1/AAF border, suggesting that, in this species, these areas may be joined along their tonotopic gradient. This is consistent with previous electrophysiological recordings from ferret MEG (Kelly et al. 1986; Phillips et al. 1988), but differs from the cat, in which A1 and AAF share a common high-frequency border (Knight 1977; Reale and Imig 1980). The two areas, A1 and AAF, could differ in other characteristics that cannot easily be determined from the optical images. For example, electrophysiological mappings suggest that, generally, AAF neurons have wider frequency-tuning curves than A1 neurons (Kowalski et al. 1995). However, tuning width is not accessible to optical imaging with the techniques used here.

In addition to A1/AAF, we observed other, as yet uncharacterized, high-frequency areas on AEG and PEG. These occur within the more ventral regions of sound-evoked 2-deoxyglucose uptake described by Wallace et al. (1997). Preliminary tracing studies have shown that they receive diffuse inputs from neurons in A1 and have different patterns of corticofugal connectivity (Bizley et al. 2003). It is likely that the auditory areas on AEG and PEG are homologous to higher-order auditory fields described in cats and other species. Although their detailed functional organization has yet to be characterized, the presence of frequency reversals in the imaging data provides valuable information about the location of these fields and suggests that any tonotopic order, if present at all, is less precise than that in A1/AAF.

GRANTS

This work was funded by the Wellcome Trust and the Medical Research Council (United Kingdom). I. Nelken was funded in part by a travel grant from the Wellcome Trust and by a McDonnell Visiting Fellowship. A. J. King is a Wellcome Senior Research Fellow, and J. K. Bizley is a Wellcome Trust Student.

REFERENCES

- Bakin JS, Kwon MC, Masino SA, Weinberger NM, and Frostig RD.** Suprathreshold auditory cortex activation visualized by intrinsic signal optical imaging. *Cereb Cortex* 6: 120–130, 1996.
- Bartfeld E and Grinvald A.** Relationships between orientation-preference pinwheels, cytochrome oxidase blobs, and ocular-dominance columns in primate striate cortex. *Proc Natl Acad Sci USA* 89: 11905–11909, 1992.
- Berne RM and Levy MN.** *Physiology*. St. Louis, MO: Mosby, 1993.
- Bizley JK, Nodal FR, Bajo VM, Moore DR, and King AJ.** Establishing cytoarchitectonic divisions in ferret auditory cortex. *Abstracts of the 26th mid-winter meeting of the Association for Research in Otolaryngology*, Daytona Beach, FL, 2003.
- Bonhoeffer T and Grinvald A.** Iso-orientation domains in cat visual cortex are arranged in pinwheel-like patterns. *Nature* 353: 429–431, 1991.
- Bonhoeffer T and Grinvald A.** Optical imaging based on intrinsic signals: the methodology. In: *Brain Mapping: The Methods*, edited by Toga AW and Mazziotta JC. San Diego, CA: Academic, 1996, p. 55–97.
- Brosch M and Schreiner CE.** Time course of forward masking tuning curves in cat primary auditory cortex. *J Neurophysiol* 77: 923–943, 1997.
- Calford MB and Semple MN.** Monaural inhibition in cat auditory cortex. *J Neurophysiol* 73: 1876–1891, 1995.
- Chapman B, Stryker MP, and Bonhoeffer T.** Development of orientation preference maps in ferret primary visual cortex. *J Neurosci* 16: 6443–6453, 1996.
- Devor A, Dunn AK, Andermann ML, Ulbert I, Boas DA, and Dale AM.** Coupling of total hemoglobin concentration, oxygenation, and neural activity in rat somatosensory cortex. *Neuron* 39: 353–359, 2003.
- Dinse HR, Godde B, Hilger T, Reuter G, Cords SM, Lenarz T, and von Seelen W.** Optical imaging of cat auditory cortex cochleotopic selectivity evoked by acute electrical stimulation of a multi-channel cochlear implant. *Eur J Neurosci* 9: 113–119, 1997.
- Frostig RD, Lieke EE, Ts'o DY, and Grinvald A.** Cortical functional architecture and local coupling between neuronal activity and the microcirculation revealed by in vivo high-resolution optical imaging of intrinsic signals. *Proc Natl Acad Sci USA* 87: 6082–6086, 1990.
- Godde B, Hilger T, von Seelen W, Berkefeld T, and Dinse HR.** Optical imaging of rat somatosensory cortex reveals representational overlap as topographic principle. *Neuroreport* 7: 24–28, 1995.
- Harel N, Mori N, Sawada S, Mount RJ, and Harrison RV.** Three distinct auditory areas of cortex (AI, AII, and AAF) defined by optical imaging of intrinsic signals. *Neuroimage* 11: 302–312, 2000.
- Harrison RV, Harel N, Kakigi A, Raveh E, and Mount RJ.** Optical imaging of intrinsic signals in chinchilla auditory cortex. *Audiol Neurootol* 3: 214–223, 1998.
- Harrison RV, Harel N, Panesar J, and Mount RJ.** Blood capillary distribution correlates with hemodynamic-based functional imaging in cerebral cortex. *Cereb Cortex* 12: 225–233, 2002.
- Heil P, Rajan R, and Irvine DRF.** Sensitivity of neurons in cat primary auditory cortex to tones and frequency-modulated stimuli. I. Effects of variation of stimulus parameters. *Hear Res* 63: 108–134, 1992.
- Hess A and Scheich H.** Optical and FDG mapping of frequency-specific activity in auditory cortex. *Neuroreport* 7: 2643–2647, 1996.
- Kalatsky VA and Stryker MP.** New paradigm for optical imaging: temporally encoded maps of intrinsic signal. *Neuron* 38: 529–545, 2003.
- Kelly JB and Judge PW.** Binaural organization of primary auditory cortex in the ferret (*Mustela putorius*). *J Neurophysiol* 71: 904–913, 1994.
- Kelly JB, Judge PW, and Phillips DP.** Representation of the cochlea in primary auditory cortex of the ferret (*Mustela putorius*). *Hear Res* 24: 111–115, 1986.
- Knight PL.** Representation of the cochlea within the anterior auditory field (AAF) of the cat. *Brain Res* 130: 447–467, 1977.
- Kowalski N, Versnel H, and Shamma SA.** Comparison of responses in the anterior and primary auditory fields of the ferret cortex. *J Neurophysiol* 73: 1513–1523, 1995.
- Logothetis NK, Pauls J, Augath M, Trinath T, and Oeltermann A.** Neurophysiological investigation of the basis of the fMRI signal. *Nature* 412: 150–157, 2001.
- Luo M and Katz LC.** Response correlation maps of neurons in the mammalian olfactory bulb. *Neuron* 32: 1165–1179, 2001.
- Malone BJ, Scott BH, and Semple MN.** Context-dependent adaptive coding of interaural phase disparity in the auditory cortex of awake macaques. *J Neurosci* 22: 4625–4638, 2002.

- Malonek D, Dirnagl U, Lindauer U, Yamada K, Kanno I, and Grinvald A.** Vascular imprints of neuronal activity: relationships between the dynamics of cortical blood flow, oxygenation, and volume changes following sensory stimulation. *Proc Natl Acad Sci USA* 94: 14826–14831, 1997.
- Martindale J, Mayhew J, Berwick J, Jones M, Martin C, Johnston D, Redgrave P, and Zheng Y.** The hemodynamic impulse response to a single neural event. *J Cereb Blood Flow Metab* 23: 546–555, 2003.
- Masino SA, Kwon MC, Dory Y, and Frostig RD.** Characterization of functional organization within rat barrel cortex using intrinsic signal optical imaging through a thinned skull. *Proc Natl Acad Sci USA* 90: 9998–10002, 1993.
- Mayhew JE, Askew S, Zheng Y, Porrill J, Westby GW, Redgrave P, Rector DM, and Harper RM.** Cerebral vasomotion: a 0.1-Hz oscillation in reflected light imaging of neural activity. *Neuroimage* 4: 183–193, 1996.
- Meister M and Bonhoeffer T.** Tuning and topography in an odor map on the rat olfactory bulb. *J Neurosci* 21: 1351–1360, 2001.
- Narayan SM, Santori EM, and Toga AW.** Mapping functional activity in rodent cortex using optical intrinsic signals. *Cereb Cortex* 4: 195–204, 1994.
- Nelken I and Versnel H.** Responses to linear and logarithmic frequency-modulated sweeps in ferret primary auditory cortex. *Eur J Neurosci* 12: 549–562, 2000.
- Nemoto M, Sheth S, Guiou M, Pouratian N, Chen JW, and Toga AW.** Functional signal- and paradigm-dependent linear relationships between synaptic activity and hemodynamic responses in rat somatosensory cortex. *J Neurosci* 24: 3850–3861, 2004.
- Phillips DP, Judge PW, and Kelly JB.** Primary auditory cortex in the ferret (*Mustela putorius*): neural response properties and topographic organization. *Brain Res* 443: 281–294, 1988.
- Phillips DP, Semple MN, Calford MB, and Kitzes LM.** Level-dependent representation of stimulus frequency in cat primary auditory cortex. *Exp Brain Res* 102: 210–226, 1994.
- Reale RA and Imig TJ.** Tonotopic organization in auditory cortex of the cat. *J Comp Neurol* 192: 265–291, 1980.
- Rubin BD and Katz LC.** Spatial coding of enantiomers in the rat olfactory bulb. *Nat Neurosci* 4: 355–356, 2001.
- Schulze H, Hess A, Ohl FW, and Scheich H.** Superposition of horseshoe-like periodicity and linear tonotopic maps in auditory cortex of the Mongolian gerbil. *Eur J Neurosci* 15: 1077–1084, 2002.
- Shamma SA, Fleshman JW, Wiser PR, and Versnel H.** Organization of response areas in ferret primary auditory cortex. *J Neurophysiol* 69: 367–383, 1993.
- Sheth SA, Nemoto M, Guiou M, Walker M, Pouratian N, and Toga AW.** Linear and nonlinear relationships between neuronal activity, oxygen metabolism, and hemodynamic responses. *Neuron* 42: 347–355, 2004.
- Shtoyerman E, Arieli A, Slovov H, Vanzetta I, and Grinvald A.** Long-term optical imaging and spectroscopy reveal mechanisms underlying the intrinsic signal and stability of cortical maps in V1 of behaving monkeys. *J Neurosci* 20: 8111–8121, 2000.
- Spitzer MW, Calford MB, Clarey JC, Pettigrew JD, and Roe AW.** Spontaneous and stimulus-evoked intrinsic optical signals in primary auditory cortex of the cat. *J Neurophysiol* 85: 1283–1298, 2001.
- Tommerdahl M, Favorov O, and Whitsel BL.** Optical imaging of intrinsic signals in somatosensory cortex. *Behav Brain Res* 135: 83–91, 2002.
- Ts'o DY, Frostig RD, Lieke EE, and Grinvald A.** Functional organization of primate visual cortex revealed by high resolution optical imaging. *Science* 249: 417–420, 1990.
- Ulanovsky N, Las L, and Nelken I.** Processing of low-probability sounds by cortical neurons. *Nat Neurosci* 6: 391–398, 2003.
- Versnel H, Mossop JE, Mrsic-Flogel TD, Ahmed B, and Moore DR.** Optical imaging of intrinsic signals in ferret auditory cortex: responses to narrowband sound stimuli. *J Neurophysiol* 88: 1545–1558, 2002.
- Wallace MN, Roeda D, and Harper MS.** Deoxyglucose uptake in the ferret auditory cortex. *Exp Brain Res* 117: 488–500, 1997.
- Weliky M and Katz LC.** Functional mapping of horizontal connections in developing ferret visual cortex: experiments and modeling. *J Neurosci* 14: 7291–7305, 1994.